

The Palomar Distant Cluster Survey :

II. The Cluster Profiles

Lori M. Lubin¹

Princeton University Observatory, Peyton Hall, Princeton NJ 08544

Marc Postman²

Space Telescope Science Institute³, 3700 San Martin Dr., Baltimore, MD 21218

Accepted for publication in the *Astronomical Journal*

¹Present Address : Observatories of the Carnegie Institution of Washington, 813 Santa Barbara St., Pasadena, CA 91101

²Guest Observer, Palomar Observatory

³Space Telescope Science Institute is operated by the Association of Universities for Research in Astronomy, Inc., under contract to the National Aeronautics and Space Administration.

ABSTRACT

We present a study of the surface density profiles of the clusters of galaxies from the Palomar Distant Cluster Survey (Postman et al. 1996). The survey contains a total of 79 clusters of galaxies, covering the estimated redshift range of $0.2 \lesssim z \lesssim 1.2$. We have analyzed the richest clusters in this sample and find that the typical Palomar cluster has a surface density profile of $r^{-1.4}$ ($r \geq 0.10 h^{-1}$ Mpc) and a core radius of $0.05 h^{-1}$ Mpc. There may be an indication that the slope of the surface density profile steepens with increasing redshift, though the observational uncertainty is at present too large to be conclusive. Our cluster population is inconsistent at a 99.9% confidence level with a population of azimuthally symmetric clusters.

Subject headings: galaxies: clustering; cosmology: observations

1. Introduction

Clusters of galaxies provide a powerful probe of the nature of galaxy formation and the origin of large scale structure in the universe. Having a well-studied sample of intermediate and high-redshift clusters is vital to understanding the evolution of galaxies and large scale structure. Because the diversity of cluster properties and the effects of evolution are significant at high redshift (Gunn & Dressler 1988; Bower et al. 1994; Castander et al. 1994; Postman et al. 1996), it is essential to sample many distant clusters with different properties. Large scale simulations have shown that cluster properties such as profile shape and substructure can constrain the nature of large scale structure formation theories and the mass density of the universe (Evrard et al. 1993; Crone, Evrard & Richstone 1995; Jing et al. 1995; Tyson & Fischer 1995). Detailed studies of these observational parameters have already been made in some individual, intermediate redshift clusters. Using weak lensing to map the mass distribution in several clusters, Smail et al. (1995) have studied two X-ray luminous clusters 1455+22 ($z = 0.26$) and 0016+16 ($z = 0.55$), Tyson & Fischer (1995) have studied Abell 1689 ($z = 0.18$), and Squires et al. (1995) have studied Abell 2218 ($z = 0.175$). All four clusters show moderate to extreme degrees of structure. However, the distribution of structure in mass, light, and X-rays are all well correlated at radii larger than $100 h^{-1}$ kpc. The projected mass density (and light) profile of A1689 can be well approximated by a power-law of $r^{-1.4 \pm 0.2}$, while the projected total mass, gas, and

light surface densities of A2218 are consistent with an isothermal sphere (r^{-1}), though perhaps slightly steeper. Smail et al. (1995) found that, while the galaxies are very good tracers of the mass, they are less concentrated, the respective core radii for 1455+22 being $r_c^{mass} = 50_{-25}^{+40} h^{-1}$ kpc and $r_c^{gal} = 90_{-25}^{+35} h^{-1}$ kpc. A multi-color photometric study of three clusters, A3284 ($z = 0.15$), A3305 ($z = 0.16$), and A1942 ($z = 0.23$), also yield consistent core radii of $r_c^{gal} \approx 120, 100,$ and $120 h^{-1}$ kpc, respectively (Molinari et al. 1994).

In this paper, we expand on these detailed analyses of individual intermediate redshift clusters by studying a large sample of intermediate and high redshift clusters from the Palomar Distant Cluster Survey (hereafter PDCS; Postman et al. 1996). We examine both the individual and global properties of the cluster profiles, specifically the cluster profile slope, core radius, and degree of asymmetry. Because the PDCS uses a completely objective and automated algorithm to detect clusters, it provides us with the largest, statistically complete sample of distant clusters. In addition, the selection biases due to the detection technique can be well quantified through simple Monte-Carlo simulations.

In §2 of this paper we briefly describe the PDCS and the cluster sample used in this analysis. The parameters of the individual cluster profiles are discussed in §3. Composite cluster profiles as a function of redshift are presented in §4. Cluster morphology is discussed in §5. We present a preliminary comparison of our results to large-scale cosmological simulations in §6 and summarize the results in §7.

2. The Cluster Sample

The cluster sample is derived from an optical/near IR survey with the 4-shooter CCD camera on the Palomar 5 meter telescope. The cluster catalog is the subject of the first paper in this series (Postman et al. 1996; hereafter Paper I). However, we discuss briefly the aspects of this catalog which are necessary for the following analysis.

The Palomar Distant Cluster Survey was conducted in two broad band filters, the F555W and F785LP of HST’s Wide Field/Planetary Camera. We denote these bands V_4 (F555W) and I_4 (F785LP) according to the convention in Paper I. The area covered consists of five one-square degree areas around the sky, all at galactic latitudes of 30 degrees or greater. The data are complete to $V_4 = 23.8$ and $I_4 = 22.5$. A matched filter algorithm was used to objectively identify the cluster candidates by using positional and photometric data simultaneously. This technique is likely to be more robust than previous optical selections which simply looked for surface density enhancements, a method which can be significantly

affected by superposition effects (*e.g.*, Gunn, Hoessel & Oke 1986; Couch et al. 1991). An advantage of this technique is that redshift estimates of the cluster candidates are produced as a byproduct of the matched filter; the main disadvantage is that we must assume a particular form for the cluster luminosity function (for the flux filter) and cluster radial profile (for the radial filter). The radial filter $P(r)$ and the flux filter $L(m)$ are given by

$$P(r) = \begin{cases} \frac{1}{\sqrt{1+(r/r_c)^2}} - \frac{1}{\sqrt{1+(r_{co}/r_c)^2}} & \text{if } r < r_{co} \\ 0 & \text{otherwise} \end{cases} \quad (1)$$

$$L(m) = \frac{\phi(m - m^*) 10^{-0.4(m-m^*)}}{b(m)} \quad (2)$$

$P(r)$ is an azimuthally symmetric cluster surface density profile which has a characteristic core radius (r_c) and which falls off at large radii as r^{-1} . The function is explicitly cut off at an arbitrary cutoff radius (r_{co}). We have chosen $r_c = 100 h^{-1}$ kpc and $r_{co} = 10 \times r_c$ such that the radial profile resembles the profiles of nearby clusters and that we have optimized the cluster detections relative to the spurious detection rates (Paper I). $\phi(m - m^*)$ is the differential Schechter luminosity function with $\alpha = -1.1$ and $M^* = -21.0$ and -21.9 in the V_4 and I_4 bands, respectively; $b(m)$ is the background galaxy counts. For the derivation of these filters and a detailed explanation, see Paper I. We have used extensive simulations in both Paper I and this paper to quantify the selection bias due to the functional form of the matched filter. We find that this selection bias has a minimal effect on the resulting distribution of profiles. The matched filter algorithm does a good job at preserving the true distribution of profile shapes for a broad range of cluster profile parameters.

Candidate clusters are detected individually in each band and then matched with each other to locate those systems which are detected in both bands. The catalog consists of 79 clusters of galaxies detected with estimated redshifts between $z \sim 0.2$ and 1.2; the uncertainty in the estimated redshift (z_{est}) is $\sigma_{z_{est}} \lesssim 0.2$ (see Paper I; Lubin 1995). 87% of the cluster candidates are matched detections (detected in both the V_4 and I_4 bands). The amplitude of the matched filter provides an estimate of the cluster richness. This filter richness (Λ_{cl}) is a measure of the effective number of L^* galaxies in the cluster (see §4.2.2 of Paper I; Lubin 1995). Through Monte-Carlo simulations, we can statistically determine the relation between Λ_{cl} and the actual cluster richness as determined by the specification of Abell (1958). This relation is dependent on profile shape; as the cluster profile slope steepens, a given Λ_{cl} value corresponds to a *lower* richness class. For a cluster which has a surface density profile of approximately r^{-1} (the assumed profile of the radial filter),

$\Lambda_{cl} \gtrsim 40$ corresponds to Abell $R \geq 1$ (Paper I). Therefore, in the analysis which follows, we will examine only those clusters with $\Lambda_{cl} \geq 40$. The cluster sample that will be the subject of this paper consists of 57 clusters in the V_4 band and 50 clusters in the I_4 band. Table 1 lists the ID number of these clusters (according to the convention of Paper I).

3. Individual Cluster Profiles

3.1. The Profile Fittings

We begin by examining the individual profiles in the V_4 and I_4 bands. We have an estimate of the cluster redshift (z_{est}) and the cluster center from the matched filter detection algorithm. The cluster center is taken to be the position of the *peak* cluster signal for each detection (see Paper I). Surface density profiles of each cluster candidate are computed by counting the number of galaxies in successive annuli around the center of each cluster. We bin out to a given *physical* radius of $1.0 h^{-1}$ Mpc (assuming $\Omega_o = 1, H_o = 100 h \text{ km s}^{-1} \text{ Mpc}^{-1}$, and $h = 0.75$) at the estimated redshift of the cluster. Twenty bins of equal radial extent are used. The uncertainty in each bin is calculated from Poisson statistics. An annulus of radii $1.0 < r \leq 1.5 h^{-1}$ Mpc around each cluster is used to measure directly the background level for each cluster. The measured background varies $\sim 10 - 15\%$ from cluster to cluster and field to field. As an example, at a redshift of $z \sim 0.5$, the number of cluster members (out to a radius of $1.0 h^{-1}$ Mpc) in a $R = 1$ cluster is ~ 150 galaxies or $10 - 20\%$ of the total number of galaxies in that region.

We quantify the slope at large radii (described by a power-law exponent α) and the cluster core radius (r_c) of the cluster profile by fitting each resulting background-subtracted surface density profile to a King model (King 1962; Cavaliere & Fusco-Femiano 1976; Sarazin & Bahcall 1977) :

$$S(r) = S_o \left[1 + \left(\frac{r}{r_c} \right)^2 \right]^{\frac{-3\beta+1}{2}} \quad (3)$$

where S_o and r_c are the normalization and core radius of the King model, respectively. β parameterizes the density fall-off at large radii; that is, the surface density profile falls off as $r^{-3\beta+1} \equiv r^{-\alpha}$.

Fig. 1 shows the distribution of power-law exponent (α) and core radii (r_c) for those cluster profiles which had acceptable fits ($\chi^2/\nu \leq 1.5; \nu = 17$). The average 1σ single

parameter errors (Avni 1976) in the fit parameters of an *individual* cluster profile are $\Delta\alpha/\alpha = {}^{+16\%}_{-12\%}$ and $\Delta r_c/r_c = {}^{+100\%}_{-60\%}$ (*e.g.*, see Table 3). We are able to constrain the slope of the surface density profile much more accurately than the cluster core radius (see also §3.2). As a consistency check, we have examined the effect on the profile fittings by (1) calculating the cluster background at a larger limiting radius; (2) changing the bin size (by $\pm 50\%$); and (3) using the *weighted* center rather than the peak center of each cluster (where the weighted center is defined as the mean position as weighted by the amplitude of the matched filter signal within the cluster detection; see also §5); the cluster fit parameters are all consistent within the measurement error with $\Delta\alpha/\alpha \lesssim 10\%$ and $\Delta r_c/r_c \lesssim 50\%$.

The variation in the cluster profile parameters is large, as is the sensitivity to the background level. Therefore, it is difficult to say anything quantitative on an individual basis (see also §4). Table 2 lists the median values and “ 1σ ” confidence interval for the *distribution* of α and r_c in each band. We define a 1σ confidence interval around each parameter by determining the points in the distribution such that the area in each tail is 16%. The average PDCS cluster has a surface density slope of $\langle\alpha\rangle \approx 1.4$ and core radius of $\langle r_c\rangle \approx 0.05 h^{-1}$ Mpc. Note that the distribution of core radii in the Palomar clusters indicates that approximately 20 – 30% of the clusters have very small or essentially no core radii (Fig. 1). The median values in the V_4 and I_4 bands are consistent with each other (Table 2).

The observed range in α is completely consistent with a sample of nearby, rich clusters ($\langle\alpha\rangle \approx 1.6$; Bahcall 1977; see also Beers & Tonry 1986; Oegerle et al. 1985; Postman, Geller & Huchra 1988), the galaxy–cluster cross correlation function which represents the *average* net galaxy density profile around rich clusters ($\langle\alpha\rangle \approx 1.2 - 1.4$; Seldner & Peebles 1977; Peebles 1980; Lilje & Efstathiou 1988), and measures of the mass (and light) distribution of intermediate redshift clusters (Smail et al. 1995; Tyson & Fischer 1995; Squires et al. 1995). The range of core radii of the PDCS clusters is also typical of other well-studied nearby and intermediate redshift clusters. A study of 15 rich, nearby clusters yields core radii of $r_c = 0.12 \pm 0.02 h^{-1}$ Mpc (Bahcall 1975; though a similar study of 12 clusters by Dressler 1978 indicate core radii larger by a factor of ~ 2). Smail et al. (1995) examined the core radii of two intermediate redshift, X-ray luminous clusters and found $r_c = 0.09^{+0.04}_{-0.03} h^{-1}$ Mpc for 1455+22 ($z = 0.26$) and $r_c \approx 0.16 h^{-1}$ Mpc for 0016+16 ($z = 0.55$), while Molinari et al. (1994) found $r_c \approx 0.10 - 0.12 h^{-1}$ Mpc for A3284 ($z = 0.15$), A3305 ($z = 0.16$), and A1942 ($z = 0.23$).

In Fig. 2, we show the cluster profiles for three matched PDCS cluster candidates (cluster ID # 003, 036 and 059; Paper I). In order to show the diversity of the PDCS clusters, we have chosen clusters which cover a range in estimated redshifts (z_{est}) and profile

shape. Table 3 lists the relevant parameters of the fittings to these cluster profiles.

3.2. Evaluating Selection Biases

In order to estimate the measurement error and to demonstrate that the matched filter does not significantly bias the profile distribution, we have performed simple Monte-Carlo simulations. We estimate the errors in our fitting procedure and evaluate the selection function by running the cluster finding algorithm on artificial fields which match, as closely as possible, the galaxy and cluster distributions of the actual PDCS fields. We reproduce our matching criteria in the cluster detection method by creating ten pairs of galaxy fields, each 1 deg^2 , as viewed through the V_4 and I_4 passbands. We accomplished this by first modeling the actual background density – magnitude function of regions of the PDCS fields which contain no detected clusters. For each simulated field, we randomly distribute the appropriate number of background galaxies in each magnitude bin according to this function. On top of this uniform field, we superimpose 25 simulated clusters with the condition that the separation between clusters must be greater than 500 arcsec. The clusters are randomly given redshifts between 0.2 and 1.2 (in z increments of 0.1) and richnesses of $R \geq 0$. The only restriction placed on cluster richness is that clusters at $z \leq 0.5$ cannot be richer than richness class 2 and clusters at $z \geq 0.6$ cannot be poorer than richness class 1. We have chosen for the cluster luminosity function the same Schechter function as the matched filter; however, we assume that half of the clusters contain spirals (and apply a Scd spiral k-correction) and half contain ellipticals (and apply an elliptical k-correction). The k-correction will affect the redshift estimate of the cluster ($\sigma_{z_{est}} \lesssim 0.2$) but not the richness estimate Λ_{cl} (Lubin 1995; Paper I).

Firstly, we estimate the *measurement* error inherent in our fitting procedure by simulating a population of clusters with a *unique* surface density slope (α) and core radius (r_c). We choose the average profile parameters observed in the PDCS : $\alpha = 1.4$ and $r_c = 0.05 h^{-1} \text{ Mpc}$. The cluster galaxies are distributed in an azimuthally symmetric manner according to the appropriate King profile (Eq. 3). We apply the same detection criteria and richness cut ($\Lambda_{cl} \geq 40$) to the simulated clusters as for the PDCS clusters. For each simulated cluster, a surface density profile is created and then fit to the King model in the manner described in §3.1. The resulting distributions of fit parameters for 20 simulated clusters are shown in Fig. 3. The median values and their 1σ errors (as defined in §3.1) of these distributions are listed in Table 4. The *median* values of the distributions of fit parameters reproduce well the actual input parameters of the simulated clusters; however,

the distributions are artificially broadened by $\sim 10\%$ in α and $\sim 50\%$ in r_c . These errors are due to uncertainties, most notably background subtraction, associated with the fitting procedure; in addition, errors in the estimated redshift contribute to the broad width of the r_c distribution. The measurement uncertainties associated with this particular cluster population are typical of the errors for cluster populations with other combinations of α and r_c .

Secondly, we examine the selection bias of the radial filter ($\alpha = 1; r_c = 0.1 h^{-1}$ Mpc) by exploring a broad range in cluster shape through two profile distributions. In the first set of simulations, we generate a Gaussian distribution of profile shapes which is reasonably close to that observed in the PDCS (Table 2); the simulated clusters have a surface density slope distribution of $\alpha = 1.4 \pm 0.6$ and a core radius distribution of $r_c = 0.05 \pm 0.05 h^{-1}$ Mpc. In the second set of simulations, we generate a Gaussian distribution of profile shapes which is very different from the PDCS, $\alpha = 2.5 \pm 0.5$ and $r_c = 0.10 \pm 0.05 h^{-1}$ Mpc. As above, the cluster galaxies are distributed in an azimuthally symmetric manner according to the appropriate King profile (Eq. 3); the same detection criteria and richness cut ($\Lambda_{cl} \geq 40$) are applied. Fig. 4 shows the input parameter distributions (shaded histograms) of the simulated clusters and the output parameter distributions (solid line histograms) of those clusters detected by the algorithm. There appears to be *no* significant selection bias in either of the two simulated cluster populations due to the matched filter; we reproduce the input distributions of α and r_c over this broad range of cluster parameters extremely well. As noted in Paper I, clusters with steeper profiles yield the strongest matched filter signal. This will affect the cluster detection probability, though the exact effect is also dependent on the cluster core radius and the cluster richness. However, we have shown with the simulations of this section that, for reasonable choices of the input cluster distribution (that is, distributions with standard deviations typical of that observed in the PDCS), the matched filter does not significantly bias the detected (output) parameter distribution.

We have quantified both the measurement error associated with the profile fitting procedure, as well as the selection bias associated with the functional form of the matched filter. The observed median parameters of the PDCS profile distributions appear to provide an accurate indication of the true parent population of cluster shapes.

3.3. Central Density – Richness Comparison

We can also estimate the slope of the cluster surface density profiles by examining the relation between richness (N_r) and central density (N_o) of the individual clusters. Similarly

to Abell (1958), central density and richness are defined as the number of member galaxies (above background) that are brighter than $m_3 + 2^m$ (where m_3 is the magnitude of the third brightest galaxy) and located within a projected radius of $0.25 h^{-1}$ Mpc and $1.0 h^{-1}$ Mpc, respectively (see §4.2.3 of Paper I for details). Fig. 5 shows N_r versus N_o for the PDCS clusters in the two passbands (top panels). The median values of N_r/N_o are $2.5_{-1.0}^{+1.0}$ (V_4 band) and $2.7_{-0.9}^{+1.4}$ (I_4 band). The standard deviation in these distributions represent 1σ confidence intervals as defined in §3.1.

The expected relation between richness and central density for the simulated cluster population described in §3.2 ($\alpha = 1.4 \pm 0.6$ and $r_c = 0.05 \pm 0.05 h^{-1}$ Mpc) is shown in the bottom panels of Fig. 5. The median values of N_r/N_o are $2.4_{-1.1}^{+1.1}$ (V_4 band) and $2.7_{-1.0}^{+1.0}$ (I_4 band), consistent with those of the PDCS. We note that the relation between N_r and N_o for a population of clusters with a much *steeper* surface density profile (*e.g.*, r^{-2} ; $\langle N_r/N_o \rangle \approx 1.6$) is inconsistent with that observed in the PDCS; the probability, as measured by the KS test, that the PDCS distribution is drawn from the same parent population as the N_r/N_o distribution of an r^{-2} cluster population is $\lesssim 10^{-12}\%$.

4. Cluster Profile Evolution

In an effort to improve our constraints on the cluster profiles, we explore the average profile shape, specifically the surface density slope α , as a function of redshift by creating global composites of our sample of PDCS clusters. Because we exclusively use estimated redshifts (observed redshifts are presently available for fewer than 10 PDCS clusters) whose uncertainty are estimated at $\sigma_{z_{est}} \lesssim 0.2$ (see §4.2.1 of Paper I), we sort each cluster by its estimated redshift (z_{est}) in V_4 and I_4 bands into three broad redshift ranges : (1) $0.2 \leq z_{est} \leq 0.4$, (2) $0.5 \leq z_{est} \leq 0.7$, and (3) $0.8 \leq z_{est} \leq 1.2$. We examine the cluster profile at $r \geq 0.10 h^{-1}$ Mpc by creating a composite cluster profile. We logarithmically bin galaxies in the radial range $0.1 \leq r \leq 1.0 h^{-1}$ Mpc around each cluster center with a bin width of 0.1 in $\log r$ (i.e. 10 bins). The background level determined for each individual cluster profile (from an outer annulus; see §3.1) is first subtracted. We stack the cluster profiles in each redshift interval according to their physical radius ($0.1 \leq r \leq 1.0 h^{-1}$ Mpc). The resulting composite cluster profiles are then fit to a power-law of the form $S(r) = S_o r^{-\alpha}$.

4.1. Composite Cluster Profiles

The composite profiles of the PDCS in the V_4 and I_4 bands are shown in Fig. 6. The redshift range is indicated in the upper right-hand corner of each panel. The error in the mean value is determined from the variance in each radius bin. The solid line indicates the best-fit power-law function. Table 5 lists the number of cluster profiles used to make the composite, the best-fit power-law slopes α , and their 1σ single parameter errors. These errors are calculated according to the procedure described by Avni (1976) who presents the correct “minimum χ^2 ” method for calculating confidence limits in a fitting with one “interesting parameter” (i.e. α). The slopes of the composite profiles are consistent with the results of the individual fittings (Table 6). The surface density slopes of the most distant clusters ($z_{est} \geq 0.8$) are slightly steeper than their intermediate redshift counterparts. This may simply reflect the larger uncertainty in the fitted parameters when co-adding such a small number of clusters (9 in V_4 band and 5 in I_4 band in this redshift interval). Such a large dispersion is also seen in the simulations when co-adding a similar number of high redshift clusters. In addition, it may be the result of a bias due to the inherent difficulty in subtracting an appropriate background for clusters at very large redshift. Nonetheless, some evolution in the cluster profile is expected for certain cosmologies (see §6).

Since richer clusters are believed to have formed at earlier epochs (Peebles 1993), we may expect to see a variation in profile shape with richness. We, therefore, examine the composite cluster profiles of a richer subset ($\Lambda_{cl} \geq 70$) of the PDCS clusters. We find that, within the observational uncertainty, there is no difference between the power-law slopes of the composites of this richer population and the composite profiles presented in Fig. 6.

4.2. Evaluating Selection Biases

In order to demonstrate that the composite profiles are not being biased by a few clusters, we performed a parametric bootstrap analysis (see Kendall & Stuart 1967). This technique involves randomly drawing a new sample (of equal number) from the original cluster sample. From each new sample, we create a composite cluster profile as described above and fit the power-law function. This procedure was performed on 50 resampled datasets. The average (and standard deviation) of the resulting α values are completely consistent (within 1σ) with the fits to the original true composite in all three redshift intervals (Table 5).

We confirm that our technique for creating cluster composites is not biased due to either the method of background subtraction or the functional form of the matched filter by performing two consistency checks. Firstly, we make composite cluster profiles

from regions of the PDCS fields which contain *no* detected clusters. For each “blank” region, we randomly assign an estimated redshift drawn from the actual estimated redshift distribution. We then bin the galaxies, subtract the background, and stack the profiles in the same manner used to create the PDCS composites. The resulting composites are shown in Fig. 7. All profiles are consistent with zero, indicating that our method of background subtraction is reasonably accurate.

Secondly, we use the simulations described in §3.2 to examine whether our cluster composites accurately reflect the mean cluster profile as a function of redshift. In an identical manner to the PDCS, we have created cluster composites from those clusters detected in 10 simulated fields. We have examined the simulated cluster population which closely resembles the PDCS clusters ($\alpha = 1.4 \pm 0.6$ and $r_c = 0.05 \pm 0.05 h^{-1}$ Mpc). The results are shown in Fig. 8. The best-fit α parameters are listed in Table 6. The resulting composite profiles of the simulated clusters are consistent with the mean slope in each redshift interval and in each band.

We have shown that our actual cluster composites (Fig. 6) are a reliable representation of the global cluster population and are not significantly biased, as a function of redshift, by the intrinsic nature of the matched filter.

5. The Cluster Morphologies

Observational studies of nearby clusters have shown that a significant portion of clusters exhibit evidence of ellipticity, multiple components, and other forms of substructure (*e.g.*, Geller & Beers 1982; Dressler & Schectman 1988; West & Bothun 1990; Jones & Forman 1992; Mohr et al. 1995; Buote & Canizares 1995; de Theije, Katgart & van Kampen 1995). Presently, measurements such as the axial ratio, centroid shift, and ellipticity have been used to quantify the cluster “morphology” (the degree of asymmetry on large scales) in the cluster surface density and X-ray contours (Mohr, Fabricant & Geller 1993; Mohr et al. 1995; Buote & Canizares 1995; de Theije et al. 1995).

We take a similar approach by examining the degree of symmetry in the PDCS clusters through the “filtered” images of the PDCS fields, i.e. the amplitude of the matched filter signal as a function of position within a given cluster detection. At each position, this signal measures how accurately a cluster centered at that position matches the filter. Since the filter is an axisymmetric, monotonically decreasing function of radius, the amplitude as a function of position is effectively a map of the structure in the cluster candidate. The

first two columns of Fig. 9 show the contour plots of sample PDCS clusters in each of the three redshift intervals (top to bottom). Adjacent panels show the contours of each cluster in the V_4 and I_4 band, respectively. The side of each panel corresponds to $2 h^{-1}$ Mpc at the estimated redshift of the cluster. The contours represent lines of constant amplitude of the matched filter signal.

We compare these contour maps with the azimuthally symmetric, centrally concentrated clusters of our simulations (§3.2). The last two columns of Fig. 9 show the contour levels of simulated clusters at the same estimated redshifts as the PDCS clusters. The simulated symmetric clusters may be marginally rounder than the PDCS clusters. We quantify any difference by measuring the offset between the *peak* center and the *weighted* center of the cluster. The peak center (used in the profile analysis) is defined as the position of the maximum signal in a given cluster detection; the weighted center is defined as the mean position as weighted by the amplitude of the matched filter signal within the cluster detection. The magnitude of this offset is a measure of the degree of asymmetry of the clusters. Fig. 10 shows the distribution of the offset (in h^{-1} kpc) for the PDCS clusters (shaded histograms) and for the azimuthally symmetric simulated clusters (solid line histograms). Using the KS test, the null hypothesis that the offset distributions are drawn from the same parent cluster population can be rejected at a 99.9% confidence level for the V_4 band and at a greater than 99.9999% confidence level for the I_4 band, indicating that the typical PDCS cluster is not azimuthally symmetric. That is, the PDCS clusters are inconsistent with an azimuthally symmetric cluster population with its characteristic α and core radius r_c . Significant structure on large scales, including ellipticity and bi-modality, in both mass, light, and X-rays have been previously found by Smail et al. (1995), Tyson & Fischer (1995) and Squires et al. (1995) in the intermediate redshift clusters 1455+22 ($z = 0.26$), 0016+16 ($z = 0.55$), Abell 1689 ($z = 0.18$), and Abell 2218 ($z = 0.175$).

6. Comparison to Structure Formation Simulations

Recently, Crone et al. (1994) and Jing et al. (1995) have used high resolution N-body simulations to examine the dependence of cosmology on the cluster mass density profile and morphology. The PDCS provides a large statistical sample to which we can compare the results of these cosmological simulations. Crone et al. (1994) examine the dependence of the cluster profile on both cosmology and initial density field by using a scale-free initial power spectra $P(k) \propto k^n$ with initial spectral indices $n = -2, -1$ and 0 for four cosmologies : Einstein deSitter ($\Omega_o = 1$), open ($\Omega_o = 0.2$ and 0.1), and flat, low-density ($\Omega_o = 0.2$,

$\Lambda_o = 0.8$). Jing et al. (1995) examined the Standard CDM model and six low-density CDM models with and without a cosmological constant. The resulting average mass density profiles are all well-fit by a power-law $\rho(r) \propto r^{-\gamma}$ for radii greater than $\sim 0.2 h^{-1}$ Mpc (or local density contrasts between 100 and 3000). There exists a clear trend toward steeper slopes with decreasing Ω_o . Crone et al. (1994) also found a correlation between steepening slopes and increasing spectral index n in their initial power spectrum. In addition, Jing et al. (1995) find that, for a given $\Omega_o (< 1)$, clusters in the flat model ($\Lambda_o = 1 - \Omega_o$) have flatter mass density profiles than in the corresponding open model. A composite of these results are presented in Fig. 11 where we plot the slope of the *surface* mass density profile ($\alpha = \gamma - 1$) versus Ω_o for simulated clusters at $z = 0$. Flat cosmologies are indicated by closed circles, while open cosmologies are indicated by open circles.

We would now like to compare the composite surface density profiles of the PDCS clusters with the cluster simulations; however, the simulations model the total mass distribution, whereas we examine the galaxy distribution. It is now possible to map the total mass density distribution as a function of radius through observations in X-rays and through gravitational lensing of rich clusters of galaxies (*e.g.*, Henry, Briel & Nulsen 1994; Smail et al. 1995; Tyson & Fischer 1995; Squires et al. 1995). These observations reveal that there is excellent agreement between the projected structure of the galaxy, gas, and dark matter distributions on scales larger than $\sim 100 h^{-1}$ kpc. Therefore, a comparison between the composite surface density profiles of the PDCS clusters with those expected from the large scale simulations should allow reasonable constraints to be placed on the mass profiles. As discussed in Tyson & Fischer (1995), our mean projected density slope of $\langle \alpha \rangle \approx 1.4$ is intermediate between standard CDM and an $\Omega_o = 0.35$ open CDM or Λ -CDM simulated profiles but appears to be a better match to the latter two. In Fig. 11, we indicate by two dotted lines the range of power-law slopes that are obtained from the composite PDCS cluster profiles over the redshift range $0.2 \lesssim z \lesssim 1.2$ (Table 5 and Fig. 6). The $\Omega_o = 1$ profiles are indeed on the low end of our observed α distribution; however, this is far from conclusive.

Up to this point there has been little examination of the evolution of cluster profile shape as a function of redshift because the cluster samples at intermediate to high redshift have been sparse. The Palomar survey provides the first statistically complete cluster survey over a large redshift range. The cluster composites may indicate that the profiles get *steeper* with increasing redshift. Such a trend in the mean slope is most prominent in the I_4 band though the trend is not significant given the large observational uncertainty. However, such an effect may also be observed in simulated clusters from high-resolution (20 kpc) N body simulations (Xu 1995). Because clusters form much later in an $\Omega_o = 1$ universe, standard CDM shows the largest evolution in the cluster profile. The slope decreases from

$\alpha = 1.51 \pm 0.27$ ($z = 1$) to $\alpha = 1.29 \pm 0.19$ ($z = 0$). The shallowing of the power-law slope at radii greater than $\sim 0.2 h^{-1}$ Mpc is largely the result of an *increase* in the cluster core radius due to continued merging between $z = 1$ and $z = 0$ (Xu 1995; Pen 1995). Profiles of clusters in an open ($\Omega_o = 0.35$) CDM shows no detectable evolution with $\alpha = 1.38 \pm 0.38$ ($z = 1$) and $\alpha = 1.38 \pm 0.19$ ($z = 0$). $\Omega_o + \Lambda$ models yield intermediate results. Other non-standard cosmologies, such as mixed dark matter models, also show a steepening of the cluster profile with redshift (Walter & Klypin 1995). At present, with little redshift information, it is not possible to use the observed variation to rule out any cosmological model.

The cluster morphology, or the degree of symmetry, has also been used to delineate between cosmological models (Evrard et al. 1993; Mohr et al. 1995; Jing et al. 1995). N-body simulations and hydrodynamic simulations show that the surface density and X-ray image contours of clusters in low-density CDM models (*e.g.*, $\Omega_o = 0.2$) are much more regular and centrally concentrated than those in an Einstein-de Sitter model ($\Omega_o = 1$). Clusters in low Ω_o cosmologies are older and are, therefore, more relaxed and symmetric than clusters in an $\Omega_o = 1$ universe. Mohr et al. (1995) have used these results to argue in favor of a flat universe, given the observed degree of asymmetry and structure in present-day clusters. Jing et al. (1995) found, however, that low- Ω_o models with a cosmological constant Λ (*e.g.*, $\Omega_o = 0.3$ and $\Lambda = 0.7$) also produce a large fraction of clusters with significant deviations from spherical symmetry, though the density and X-ray image contours are still rounder than the $\Omega_o = 1$ case. However, this matter is still controversial as Pen (1995) and Xu (1995) find little quantitative difference in the structure characteristics of clusters formed in these cosmological models. We have used the contours of constant amplitude of the matched filter signal to examine the degree of symmetry in the PDCS clusters. We do find that the PDCS clusters are inconsistent with a population of azimuthally symmetric simulated clusters (Fig. 10).

7. Summary

We have examined the galaxy distributions of the richest clusters of galaxies from the Palomar Distant Cluster Survey. Through an analysis of individual cluster profiles and composite profiles as a function of redshift, we find that the typical Palomar cluster has a profile of $r^{-1.4}$ at radii greater than $0.10 h^{-1}$ Mpc and a core radius of $0.05 h^{-1}$ Mpc. The distribution of core radii in the Palomar clusters indicates that up to 30% of the clusters have very small or essentially no core radii. Using simple Monte-Carlo simulations, we have

shown that the median cluster profile parameters appear to be an accurate representation of the actual cluster population; the measurement errors associated with these parameters are $\sim 10\%$ in the surface density slope α and $\sim 50\%$ in the cluster core radius r_c . The average profile parameters of the PDCS clusters are consistent with measures of nearby clusters, as well as other intermediate redshift clusters (Molinari et al. 1994; Tyson & Fischer 1995; Squires et al. 1995; Smail et al. 1995). There may be an indication that the mean cluster profile steepens with increasing redshift, though the observational uncertainty is presently too large to be conclusive. In addition, we find that a large fraction of the PDCS clusters have a significant degree of asymmetry. The PDCS cluster population is inconsistent with a population of circularly symmetric clusters of galaxies at a greater than 99.9% confidence level.

We thank the anonymous referee for comments which greatly improved this paper. We gratefully acknowledge the useful discussions with Neta Bahcall, Jim Gunn, Robert Lupton, David Spergel, and Michael Strauss. We also thank Sangeeta Malhotra for her library of SM macros, Bob Rutledge for his incredible fitting program BFIT, and Ue-Li Pen and Guohong Xu for preliminary results of their cosmological simulations. This work is supported in part by NASA contract NGT-51295 (LML).

REFERENCES

- Abell, G.O. 1958, *ApJS*, 232, 689
- Avni, Y. 1976, *ApJ*, 210, 642
- Bahcall, N.A. 1975, *ApJ*, 198, 249
- Bahcall, N.A. 1977, *ARA&A*, 15, 505
- Beers, T.C. & Tonry, J.L. 1988, *ApJ*, 300, 557
- Bower, R.G., Boehringer, H., Briel, U.G., Ellis, R.G., Castander, F.J., & Couch, W.J. 1994, *MNRAS*, 286, 345
- Buote, D.A. & Canizares, C.R. 1996, *ApJ*, to appear February 1 issue
- Castander, F.J., Ellis, R.S., Frenk, C.S., Dressler, A. & Gunn, J.E. 1994 *ApJ*, 424, L79
- Cavaliere, A. & Fusco-Femiano, R. 1976, *A&A*, 49, 137
- Crone, M.M., Evrard, A.E. & Richstone, D.O. 1994, *ApJ*, 434, 402
- Couch, W.J., Ellis, R.S., Malin, D.F., & MacLaren, I. 1991, *MNRAS*, 249, 606
- de Theije, P.A.M., Katgert, P. & van Kampen, E. 1995, *MNRAS*, 273, 30
- Dressler, A. 1978, *ApJ*, 226, 55
- Dressler, A. & Schectman, S.A. 1988, *AJ*, 95, 985
- Evrard, A.E., Mohr, J.J., Fabricant, D.J. & Geller, M.J. 1993, *ApJ*, 419, L9
- Geller, M.J. & Beers, T.C. 1982, *PASP*, 92, 421
- Gunn, J.E., Hoessel, J. & Oke, J.B. 1986, *ApJ*, 306, 30
- Gunn, J.E. & Dressler, A. 1988, *Towards Understanding Galaxies at Large Redshift*, R. Kron and A. Renzini, eds., Dordrecht, p. 29
- Henry, J.P., Briel, U.G. & Nulsen, P.E.J. 1993, *A&A*, 271, 413
- Jing, Y.P., Mo, H.J., Börner, G. & Fang, L.Z. 1995, *MNRAS*, 276, 417
- Jones, C. & Forman, W. 1992, *Clusters and Superclusters of Galaxies*, ed. A.C. Fabian, NATO ASI Series 366, Kluwer Academic Publishers
- Kendall, M.G. & Stuart, A. 1967, *Advanced Theory of Statistics* (New York: Hafner)
- King, I.R. 1962, *ApJ*, 62, 471
- Lilje, P.B. & Efstathiou, G. 1988, *MNRAS*, 231, 635
- Lubin, L.M. 1995, PhD Thesis, Princeton University

- Mohr, J.J., Fabricant, D.G. & Geller, M.J. 1993, ApJ, 413, 492
- Mohr, J.J., Evrard, A.E., Fabricant, D.G. & Geller, M.J. 1995, ApJ, 447, 8
- Molinari, E., Banzi, M., Buzzoni, G., Chincarini, G. & Pedrana, M.D. 1994, A&AS, 103, 245
- Oegerle, W.R., Hoessel, J.G. & Jewison, M.S. 1987, AJ, 93, 519
- Peebles, P.J.E. 1980, *The Large Scale Structure of the Universe* (Princeton: Princeton Univ Press)
- Peebles, P.J.E. 1993, *Physical Cosmology* (Princeton: Princeton Univ Press)
- Pen, U. 1995, private communication
- Postman, M., Geller, M.J. & Huchra, J.P. 1988, AJ, 95, 267
- Postman, M., Lubin, L.M., Gunn, J.E., Oke, J.B., Schneider, D.P., Hoessel, J.G. & Christensen, J.A. 1996, AJ, to appear in February 1996 issue (Paper I)
- Sarazin, C.L. & Bahcall, J.N. 1977, ApJS, 34, 451
- Seldner, M. & Peebles, P.J.E. 1977, ApJ, 215, 703
- Smail, I., Ellis, R., Fitchett, M. & Edge, A.C. 1995, MNRAS, 273, 277
- Squires, G., Kaiser, N., Babul, A., Fahlman, G., Woods, D., Neumann, D.M. & Böhringer, H. 1995, ApJ, submitted
- Tyson, J.A. & Fischer, P. 1995, ApJ, 446, L55
- Walter, C. & Klypin, A. 1995, preprint
- West, M.J. & Bothun, G.D. 1990, ApJ, 350, 36
- Xu, G. 1995, private communication

Figure Captions

Figure 1 : Distribution of surface density slopes (α) and core radii (r_c in h^{-1} Mpc) from the fittings to the PDCS cluster profiles. The shaded and solid line histograms represent the distribution of parameters from individual profile fittings of the PDCS clusters for the V_4 and I_4 bands, respectively. We show only those fittings which have acceptable χ^2/ν (see §3.1).

Figure 2 : King profile fittings to three matched cluster candidates. Adjacent panels show the cluster profile in the V_4 and I_4 bands, respectively. The estimated redshift (z_{est}) and the cluster ID number is indicated in the top right and left of each panel, respectively. A solid line indicates the best-fit King model (Eq. 3).

Figure 3 : Distribution of surface density slopes (α) and core radii (r_c in h^{-1} Mpc) from the fittings to the profiles of a simulated cluster population with a discrete α and r_c combination ($\alpha = 1.4$; $r_c = 0.05 h^{-1}$ Mpc). The median values accurately reproduce the actual profile parameters, though the distributions are artificially broadened due to inherent errors in the fitting process (see §3.2).

Figure 4 : The input (shaded histograms) and output (solid line histograms) distributions of surface density slopes (α ; top panels) and core radii (r_c in h^{-1} Mpc; bottom panels) of the two sets of simulated clusters (see §3.2). The input parameter distributions are specified in the upper right-hand corner of each panel. All distributions are shown separately for the V_4 and I_4 bands.

Figure 5 : Abell richness N_r ($\leq 1.0 h^{-1}$ Mpc) versus central density N_o ($\leq 0.25 h^{-1}$ Mpc) for the PDCS clusters and for simulated clusters (see §3.2) in the V_4 and I_4 bands. The black dots, open squares, and stars indicate clusters detected at estimated redshifts of $0.2 \leq z_{est} \leq 0.4$, $0.5 \leq z_{est} \leq 0.7$, and $z_{est} \geq 0.8$, respectively. The expected relation from the simulations is consistent with the observations.

Figure 6 : Composite surface density profiles ($0.10 \leq r \leq 1.0 h^{-1}$ Mpc) of the PDCS clusters. The clusters have been divided in three redshift bins based upon their estimated redshifts in each band. The individual background surface density has been subtracted from each individual cluster profile before creating the composite. The variance in each bin is used to compute the error in the mean value. The best-fit power-law functions are shown.

Figure 7 : Composite surface density profiles ($0.1 \leq r \leq 1.0 h^{-1}$ Mpc) of regions in the PDCS fields which contain no detected clusters. We have assumed estimated

redshifts such that we have roughly the same number of profiles in each redshift bin as the real cluster composites (Fig. 6). The constant background surface density has been subtracted from each “profile” before creating the composite. All profiles are consistent with zero, indicating that our method of background subtraction is reasonably accurate.

Figure 8 : Composite surface density profiles ($0.1 \leq r \leq 1.0 h^{-1}$ Mpc) of the simulated clusters. The clusters have been divided in three redshift bins based upon their estimated redshifts in each band. The constant background surface density has been subtracted from each individual cluster profile before creating the composite. The variance in each bin is used to compute the error in the mean value. The best-fit power-law functions are shown.

Figure 9 : Contour maps of the amplitude of the matched filter signal in both bands for one cluster in each of the three redshift intervals (top panel $0.2 \leq z_{est} \leq 0.4$; middle panel $0.5 \leq z_{est} \leq 0.7$; bottom panel $0.8 \leq z_{est} \leq 1.2$). The first two columns show actual PDCS clusters, and the last two columns show azimuthally symmetric, simulated clusters. The side of each panel corresponds to $2 h^{-1}$ Mpc at the estimated redshift of the cluster.

Figure 10 : Distribution of offsets (in h^{-1} kpc) between the peak center (the position of the maximum signal of the matched filter) and the weighted center. The shaded histograms represent the distribution of offsets of the PDCS clusters. The solid line histograms represent the distribution of offsets of the azimuthally symmetric, simulated clusters. The distributions are shown separately for the V_4 and I_4 bands. The actual data and the simulations are statistically different (see §5).

Figure 11 : The expected power-law slopes of the cluster *mass* surface density profiles versus Ω_o from various cosmological simulations (Crone et al. 1994; Jing et al. 1995). Open and closed circles indicate open and flat cosmologies, respectively, and represent simulated clusters at $z = 0$. Dashed lines indicate the range of power-law slopes of the composite PDCS cluster *galaxy* profiles over our full redshift interval $0.2 \lesssim z \lesssim 1.2$ (Table 5).

Table 1 : The Sample of PDCS Clusters

Band	PDCS Cluster ID Number																																																								
V_4	001	002	003	004	006	008	010	011	012	015	016	017	018	019	020	021	022	023	024	025	027	030	031	033	034	035	036	037	038	039	041	042	044	047	048	049	050	051	052	053	054	055	056	057	059	062	063	065	066	067	068	069	071	072	075	076	078
I_4	001	002	003	004	006	008	009	010	011	012	014	015	016	017	018	019	020	021	022	023	024	031	033	034	035	036	037	039	041	042	045	049	050	051	052	054	055	056	057	059	061	062	063	064	067	068	069	075	076	079							

Table 2 : Median Values of Surface Density Slope α and Core Radius r_c (h^{-1} Mpc) of the PDCS Clusters

Band	#	α	r_c
V_4	43	$1.36^{+1.12}_{-0.47}$	$0.05^{+0.12}_{-0.04}$
I_4	37	$1.35^{+1.07}_{-0.35}$	$0.05^{+0.10}_{-0.03}$

Table 3 : Surface Density Slope α and Core Radius r_c (h^{-1} Mpc) of Three Matched PDCS Clusters

Panel	PDCS	V_4		I_4	
	ID #	α	r_c	α	r_c
Top	036	$1.72^{+0.39}_{-0.23}$	$0.03^{+0.04}_{-0.02}$	$2.53^{+0.69}_{-0.42}$	$0.21^{+0.46}_{-0.11}$
Middle	003	$1.79^{+0.66}_{-0.42}$	$0.35^{+0.05}_{-0.29}$	$1.23^{+0.18}_{-0.13}$	$0.04^{+0.03}_{-0.02}$
Bottom	059	$2.13^{+0.75}_{-0.39}$	$0.04^{+0.25}_{-0.02}$	$2.42^{+0.51}_{-0.30}$	$0.04^{+0.04}_{-0.02}$

Table 4 : Measurement Error Associated with Median Values of Surface Density Slope α and Core Radius r_c (h^{-1} Mpc) from the Simulated Clusters

Band	α	r_c
V_4	$1.36^{+0.12}_{-0.23}$	$0.057^{+0.032}_{-0.015}$
I_4	$1.43^{+0.12}_{-0.15}$	$0.059^{+0.032}_{-0.027}$

Table 5 : Power-Law Slopes of Composite Surface Density Profiles of the PDCS Clusters

Redshift Interval	V_4		I_4	
	#	α	#	α
$0.2 \leq z_{est} \leq 0.4$	26	$1.50^{+0.22}_{-0.34}$	21	$1.32^{+0.13}_{-0.18}$
$0.5 \leq z_{est} \leq 0.7$	22	$1.34^{+0.18}_{-0.27}$	24	$1.66^{+0.16}_{-0.24}$
$0.8 \leq z_{est} \leq 1.2$	9	$2.06^{+0.24}_{-0.43}$	5	$1.93^{+0.19}_{-0.24}$

Table 6 : Power-Law Slopes of Composite Surface Density Profiles of the Simulated Clusters

Redshift Interval	V_4		I_4	
	#	α	#	α
$0.2 \leq z_{est} \leq 0.4$	29	$1.46^{+0.15}_{-0.20}$	29	$1.47^{+0.15}_{-0.19}$
$0.5 \leq z_{est} \leq 0.7$	66	$1.49^{+0.15}_{-0.20}$	71	$1.45^{+0.12}_{-0.16}$
$0.8 \leq z_{est} \leq 1.2$	45	$1.37^{+0.25}_{-0.55}$	53	$1.44^{+0.15}_{-0.20}$

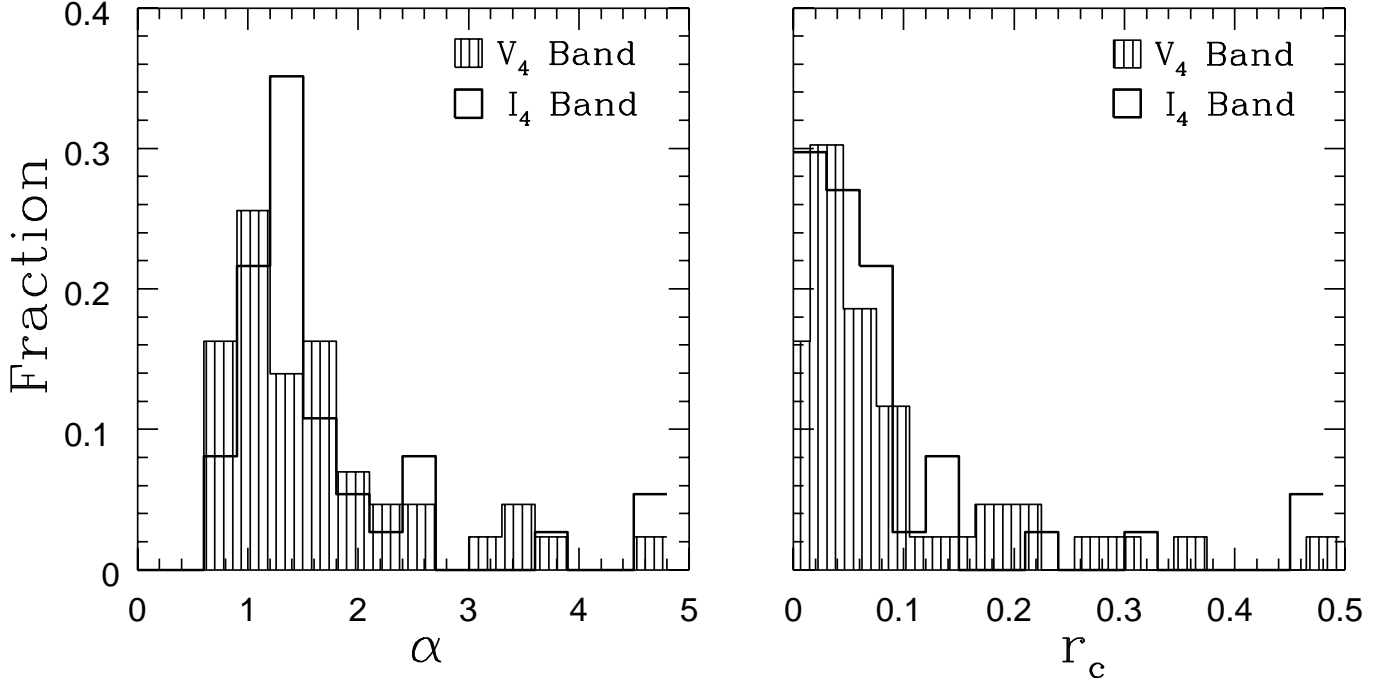


Fig. 1.— Distribution of surface density slopes (α) and core radii (r_c in h^{-1} Mpc) from the fittings to the PDCS cluster profiles. The shaded and solid line histograms represent the distribution of parameters from individual profile fittings of the PDCS clusters for the V_4 and I_4 bands, respectively. We show only those fittings which have acceptable χ^2/ν (see §3.1).

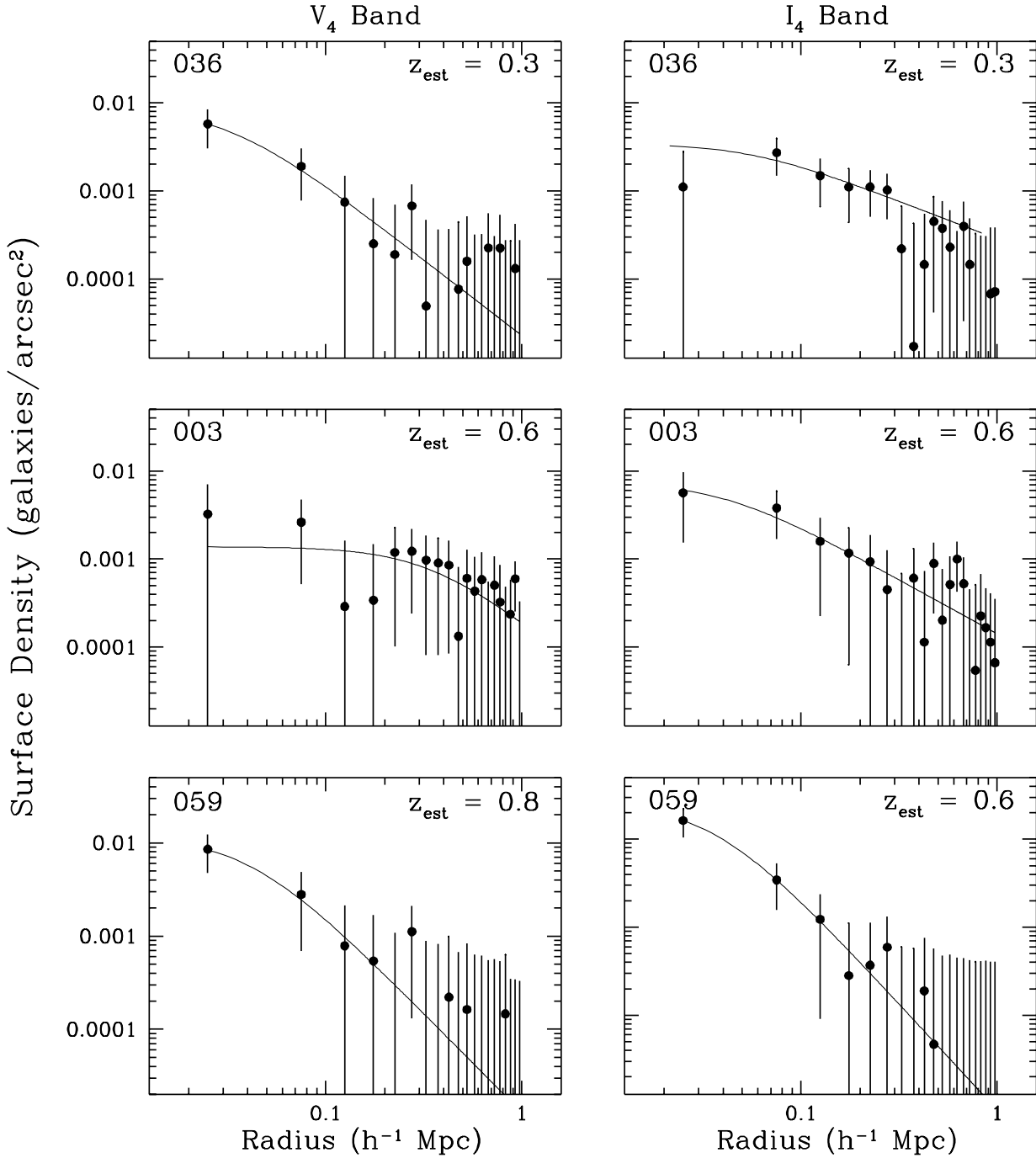


Fig. 2.— King profile fittings to three matched cluster candidates. Adjacent panels show the cluster profile in the V_4 and I_4 bands, respectively. The estimated redshift (z_{est}) and the cluster ID number is indicated in the top right and left of each panel, respectively. A solid line indicates the best-fit King model (Eq. 3).

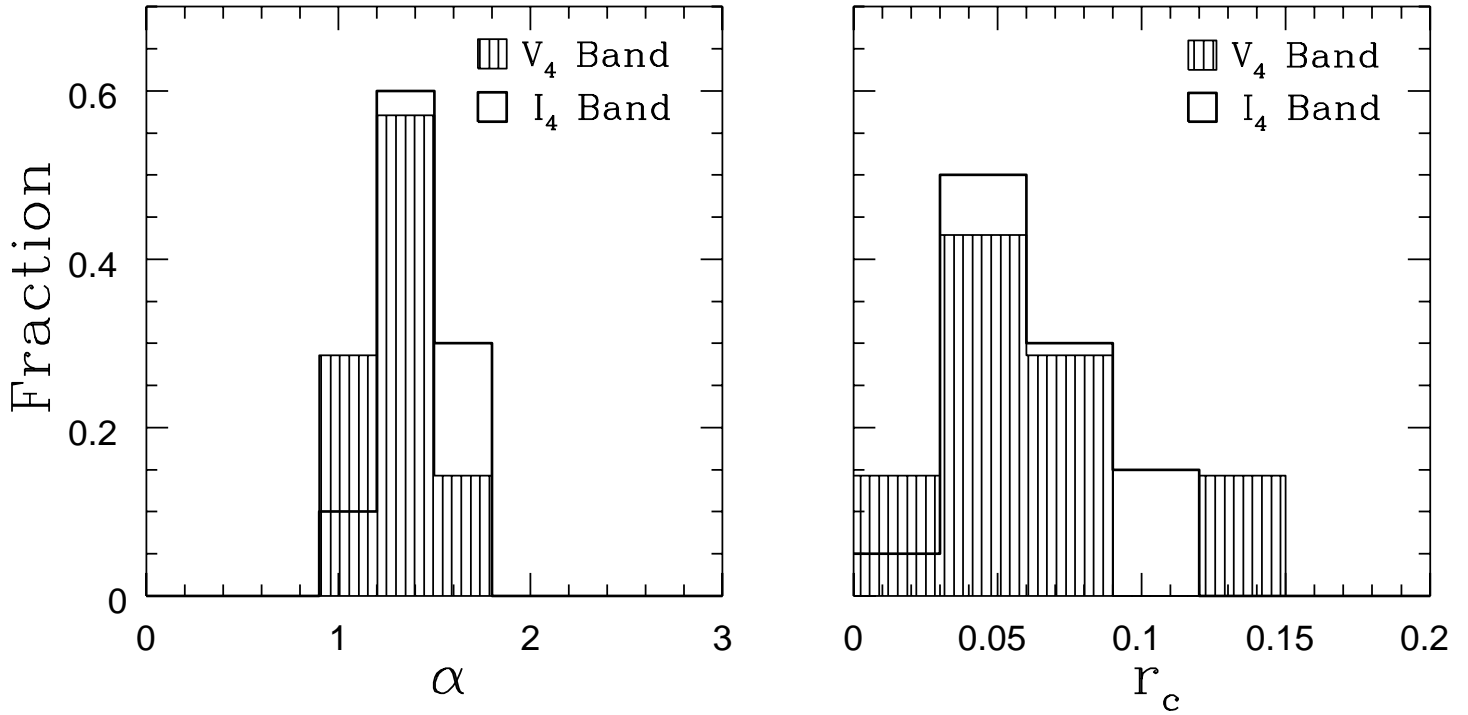


Fig. 3.— Distribution of surface density slopes (α) and core radii (r_c in h^{-1} Mpc) from the fittings to the profiles of a simulated cluster population with a discrete α and r_c combination ($\alpha = 1.4$; $r_c = 0.05 h^{-1}$ Mpc). The median values accurately reproduce the actual profile parameters, though the distributions are artificially broadened due to inherent errors in the fitting process (see §3.2).

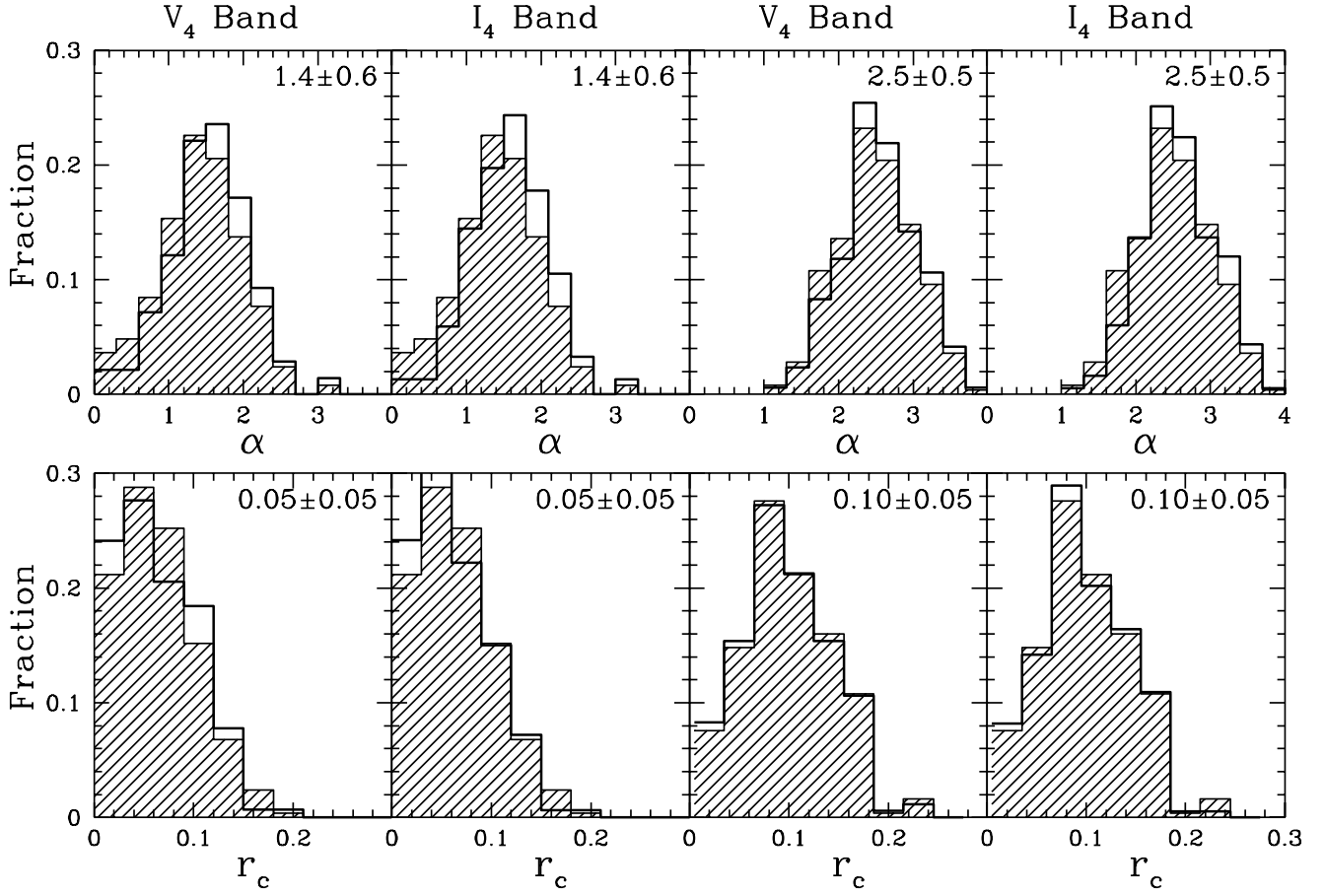


Fig. 4.— The input (shaded histograms) and output (solid line histograms) distributions of surface density slopes (α ; top panels) and core radii (r_c in h^{-1} Mpc; bottom panels) of the two sets of simulated clusters (see §3.2). The input parameter distributions are specified in the upper right-hand corner of each panel. All distributions are shown separately for the V_4 and I_4 bands.

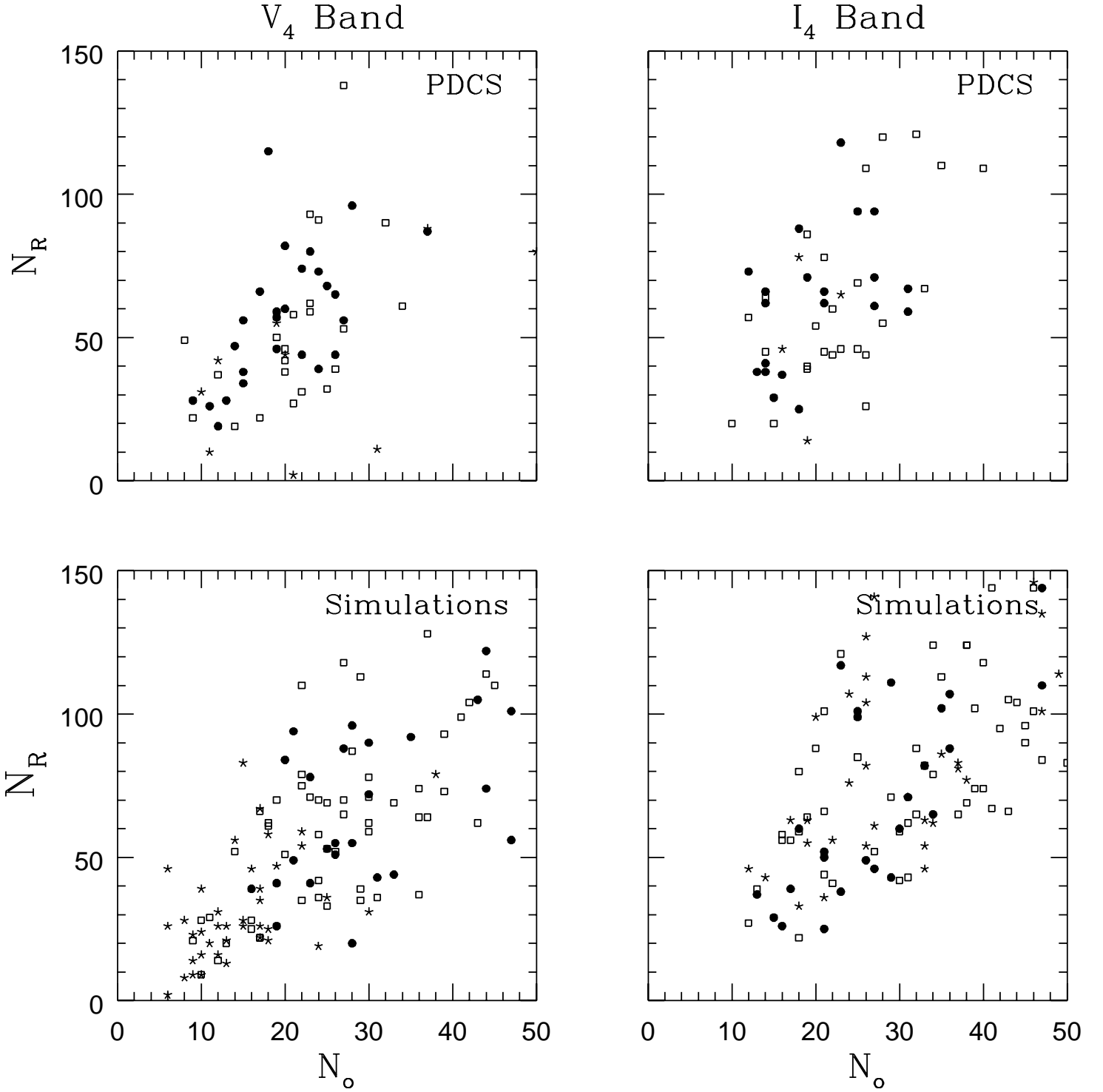


Fig. 5.— Abell richness N_r ($\leq 1.0 h^{-1}$ Mpc) versus central density N_o ($\leq 0.25 h^{-1}$ Mpc) for the PDCS clusters and for simulated clusters (see §3.2) in the V_4 and I_4 bands. The black dots, open squares, and stars indicate clusters detected at estimated redshifts of $0.2 \leq z_{est} \leq 0.4$, $0.5 \leq z_{est} \leq 0.7$, and $z_{est} \geq 0.8$, respectively. The expected relation from the simulations is consistent with the observations.

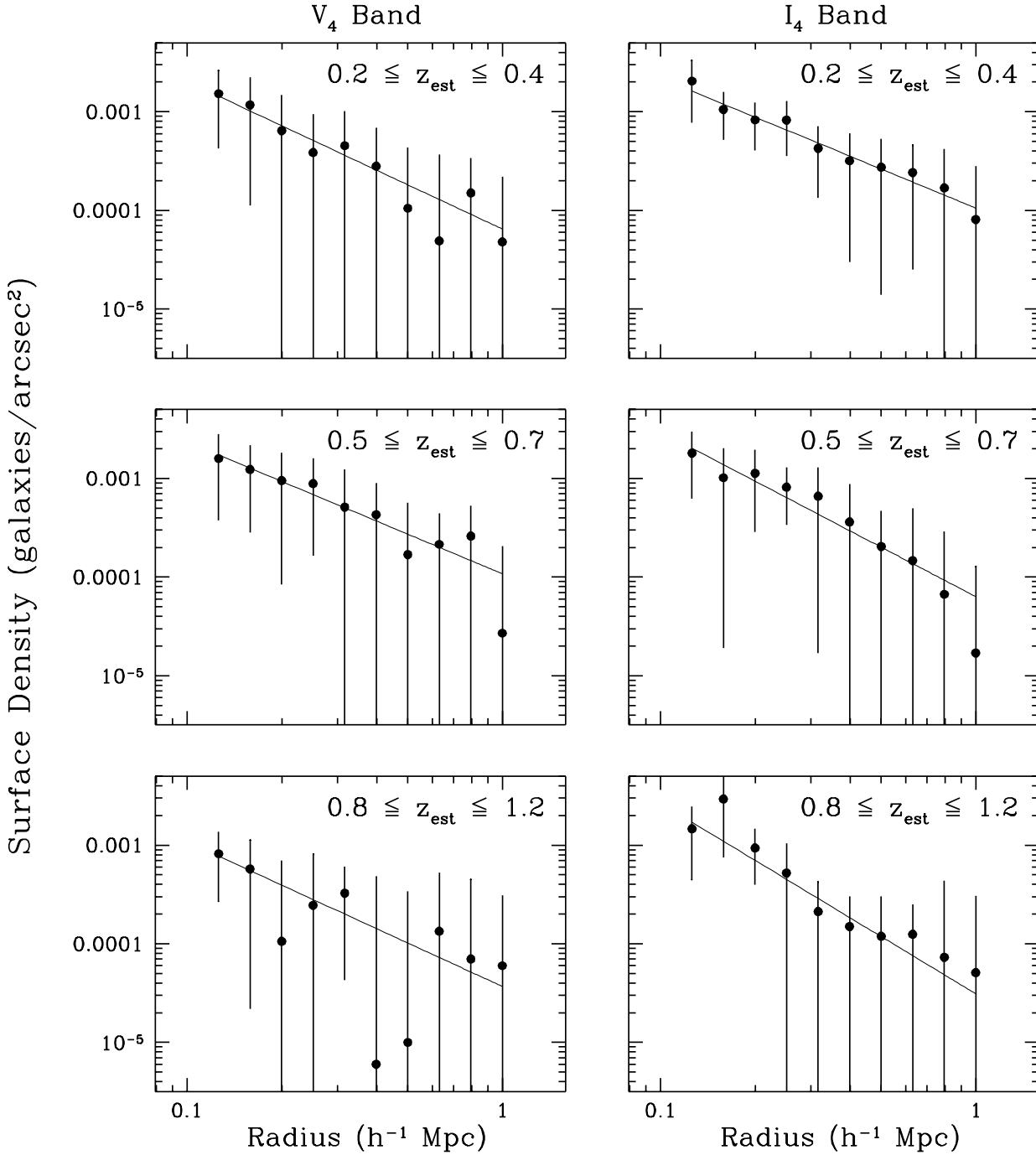


Fig. 6.— Composite surface density profiles ($0.10 \leq r \leq 1.0 h^{-1} \text{ Mpc}$) of the PDCS clusters. The clusters have been divided in three redshift bins based upon their estimated redshifts in each band. The individual background surface density has been subtracted from each individual cluster profile before creating the composite. The variance in each bin is used to compute the error in the mean value. The best-fit power-law functions are shown.

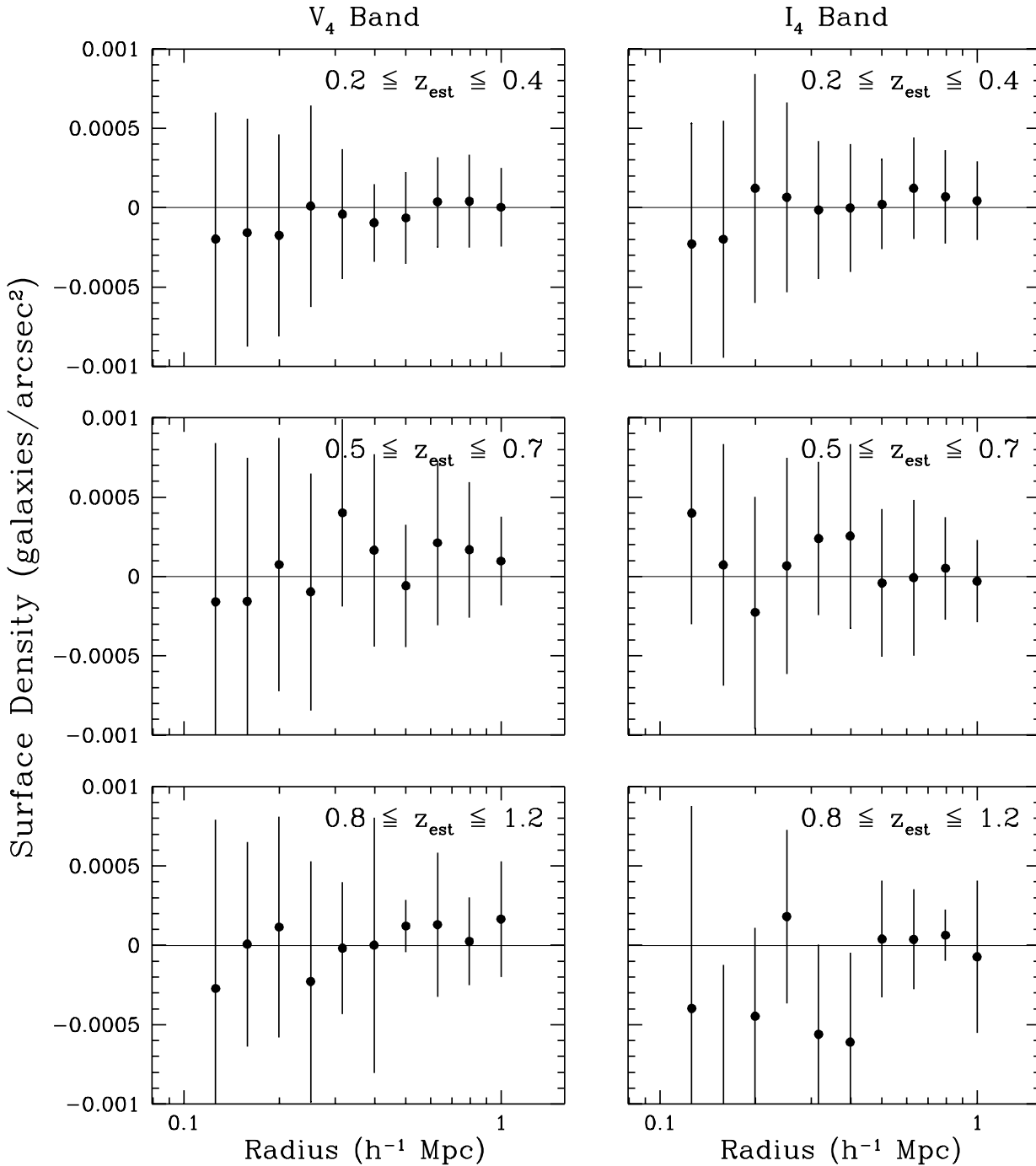


Fig. 7.— Composite surface density profiles ($0.1 \leq r \leq 1.0 h^{-1}$ Mpc) of regions in the PDCS fields which contain no detected clusters. We have assumed estimated redshifts such that we have roughly the same number of profiles in each redshift bin as the real cluster composites (Fig. 6). The constant background surface density has been subtracted from each “profile” before creating the composite. All profiles are consistent with zero, indicating that our method of background subtraction is reasonably accurate.

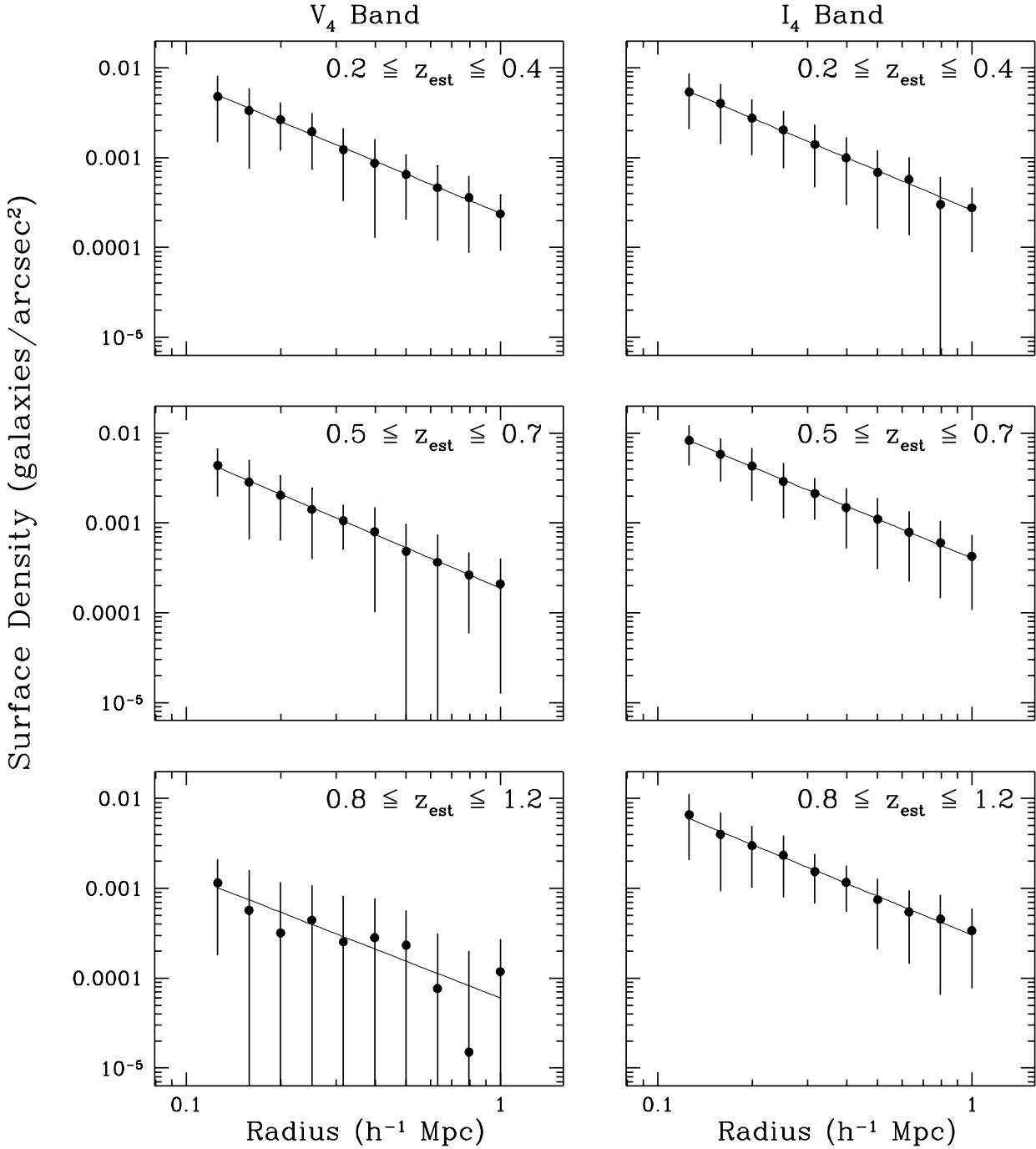


Fig. 8.— Composite surface density profiles ($0.1 \leq r \leq 1.0 h^{-1}$ Mpc) of the simulated clusters. The clusters have been divided in three redshift bins based upon their estimated redshifts in each band. The constant background surface density has been subtracted from each individual cluster profile before creating the composite. The variance in each bin is used to compute the error in the mean value. The best-fit power-law functions are shown.

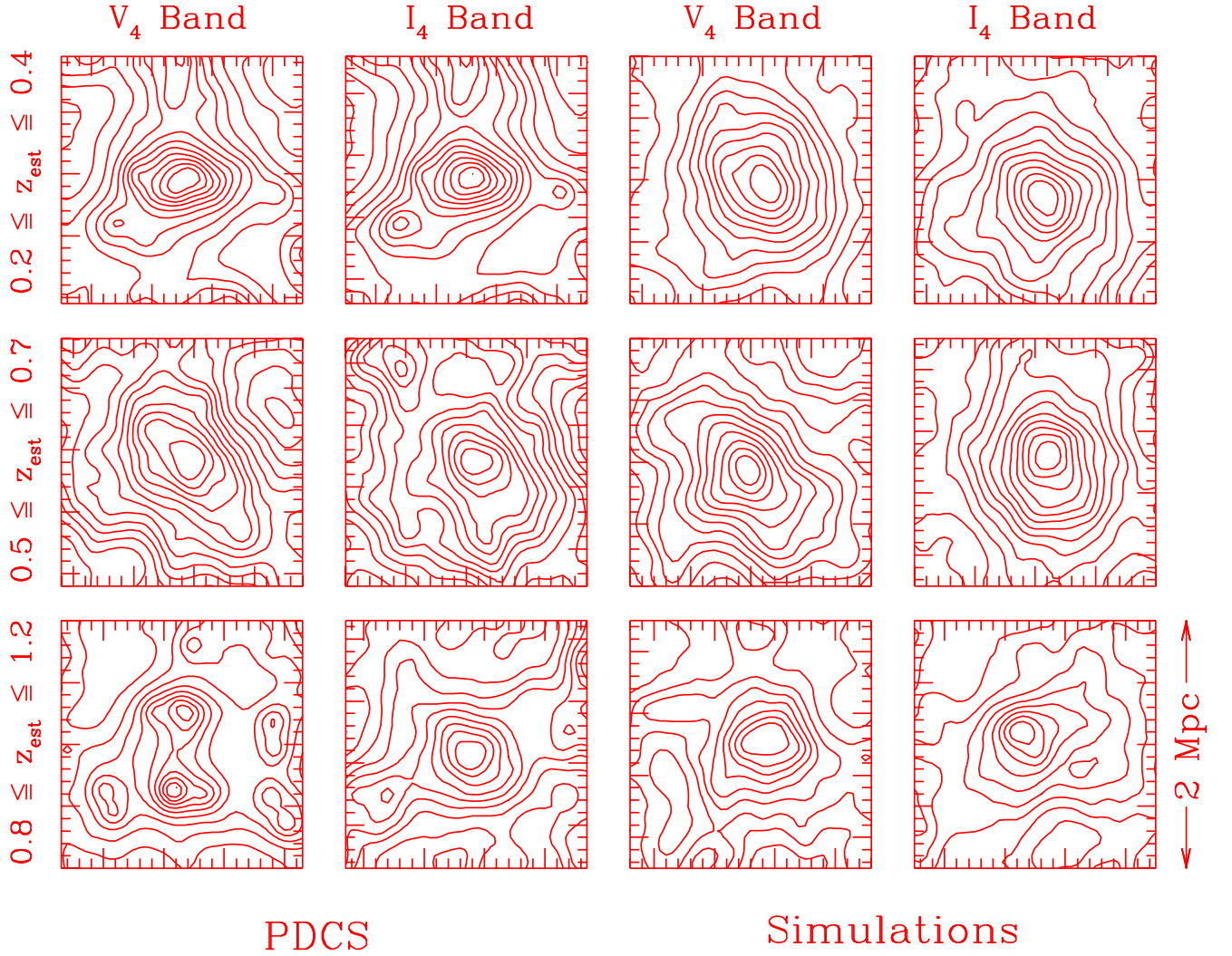


Fig. 9.— Contour maps of the amplitude of the matched filter signal in both bands for one cluster in each of the three redshift intervals (top panel $0.2 \leq z_{est} \leq 0.4$; middle panel $0.5 \leq z_{est} \leq 0.7$; bottom panel $0.8 \leq z_{est} \leq 1.2$). The first two columns show actual PDCS clusters, and the last two columns show azimuthally symmetric, simulated clusters. The side of each panel corresponds to $2 h^{-1}$ Mpc at the estimated redshift of the cluster.

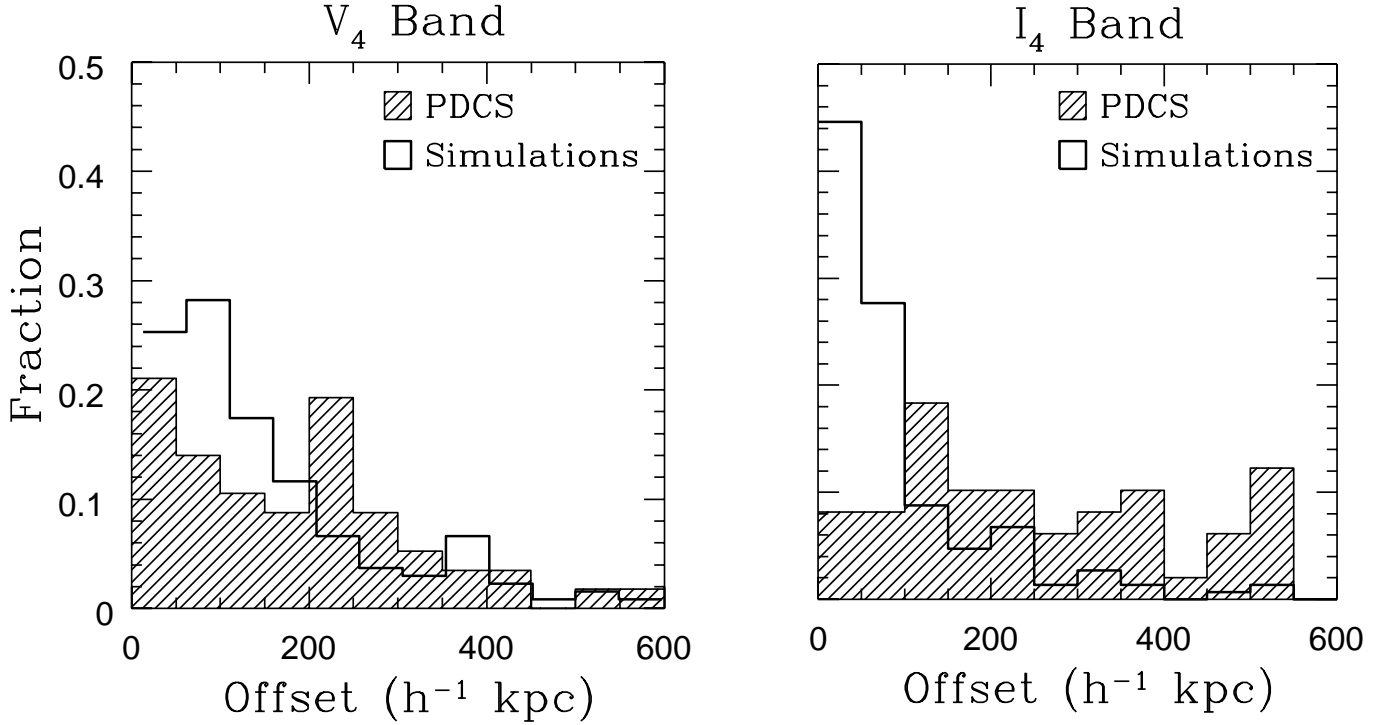


Fig. 10.— Distribution of offsets (in h^{-1} kpc) between the peak center (the position of the maximum signal of the matched filter) and the weighted center. The shaded histograms represent the distribution of offsets of the PDCS clusters. The solid line histograms represent the distribution of offsets of the azimuthally symmetric, simulated clusters. The distributions are shown separately for the V_4 and I_4 bands. The actual data and the simulations are statistically different (see §5).

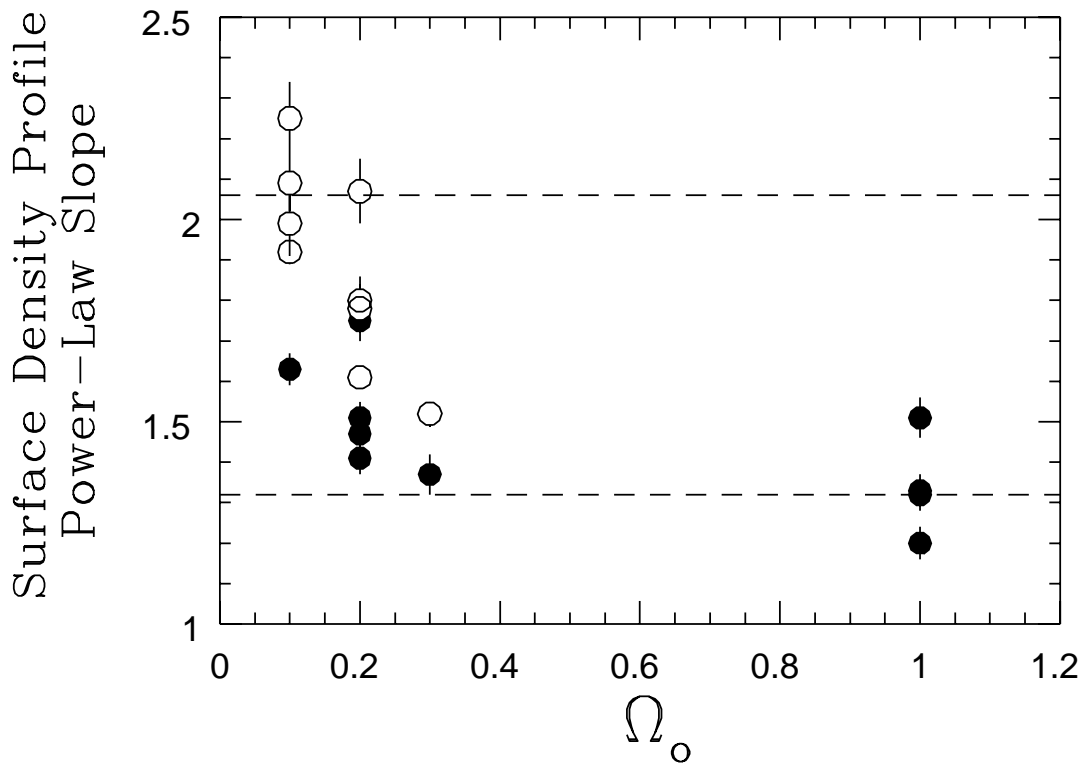


Fig. 11.— The expected power-law slopes of the cluster *mass* surface density profiles versus Ω_0 from various cosmological simulations (Crone et al. 1994; Jing et al. 1995). Open and closed circles indicate open and flat cosmologies, respectively, and represent simulated clusters at $z = 0$. Dashed lines indicate the range of power-law slopes of the composite PDCS cluster *galaxy* profiles over our full redshift interval $0.2 \lesssim z \lesssim 1.2$ (Table 5).